

Spreading and Migration of Nasopharyngeal Normal and Cancer Cells on Microgratings

Yi Liu,[¶] Jifeng Ren,[¶] Ruolin Zhang, Shuhuan Hu, Stella W. Pang,* and Raymond H. W. Lam*Cite This: *ACS Appl. Bio Mater.* 2021, 4, 3224–3231

Read Online

ACCESS |



Metrics & More



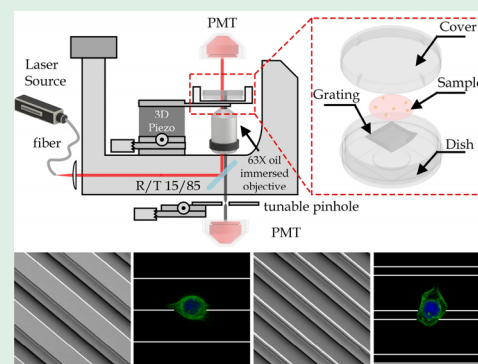
Article Recommendations



Supporting Information

ABSTRACT: Cell spreading and migration play a pivotal role in many diseases such as tumor metastasis. In particular, nasopharyngeal tumor cells have known of their tendency of migration to pterygoid muscles and further distant metastasis. Although existing studies revealed key characteristics of the nasopharyngeal tumor cells, their migration preference is yet to be thoroughly understood, especially in the physical aspects including the microtopographical factors. Researchers have developed techniques in recent years to study microtopography-related cell behaviors but they are not yet applied in investigating the nasopharyngeal tumor cells. In this work, we elaborate the spreading and migration characteristics of normal and cancerous nasopharyngeal cells on micrograting substrates mimicking the microtopography of myotubes of the pterygoid muscles. We further apply interference reflection microscopy (IRM) to visualize the cell–substrate adhesion dynamics. We are interested in examining the microtopography-related cell spreading and migration behaviors and their correlations, providing insights for deeper understanding and more promising prediction on the nasopharyngeal tumor metastasis.

KEYWORDS: cell spreading, migration, microgratings, nasopharynx cancer, correlation



INTRODUCTION

Nasopharyngeal carcinoma (NPC) is a prevalent endemic disease in Southeast Asia with high rate of invasion and distance metastasis.¹ It has been reported that 4–10% of NPC patients present synchronous metastasis (smNPC) at their initial diagnosis.² With advancement in medical imaging and diagnosis techniques, substantial clinical data indicates that the tumor cells invade into the space around the pharynx and nearby muscles or even exhibit metastasis and spread to distant sites (e.g., liver and lungs) in the metaphase (stage II~III) NPC patients.^{3–5} Moreover, the eighth edition of the “Tumor, Nodes and Metastases” (TNM) staging system (2016) has considered the tumor extension into the pterygoid muscles (T2) as a basis for staging classification.⁶ Although there are biomarkers such as Epstein–Barr virus (EBV)-expressed miRNA (i.e., *BamHI-A* rightward transcripts) and metastatic tumor antigen 1 (MTA1) for indicating NPC pathogenesis and metastasis, the underlying mechanism that prompting NPC exhibit such invasive and metastatic behavior is still undetermined.⁷ Further, many clinical evidence indicate that NPC invasion and metastasis can cause pathologic change of muscle tissues and even muscular necrosis.^{8–10} It is important to investigate the cancer cells’ behaviors when attaching to a new colony (i.e., pterygoid muscles) and proliferate to form secondary tumors.

There are increasing studies reported cell behaviors such as migration and adhesion are closely associated with cancer

metastasis and progression.^{11,12} The key steps in metastasis are elucidated as the cancer cell will first detach from the primary tumor and undergo migration, invasion, and traveling through the vein, then finally adhesion at the new site.¹³ In fact, these cell fundamental behaviors can influence the rate of secondary tumor colony establishment. Taking intravasation for example, a small subpopulation of primary tumor cells tends to adhere on endothelial cells, following by migrating through endothelial cell layer such that they can eventually become circulating tumor cells in blood vessels.^{14,15} Therefore, the characteristics of cell attachment and migration can reflect potential tumor metastasis ability and cell malignant-related tendency.

To demonstrate the cell behavior studies on tissues with different micro/nanotopography in vitro, many attempts have been reported in the past decades. Lewis et al. performed skeletal muscle tissue culture in vitro back in 1910.¹⁶ Later in 1990s, the first three-dimensional muscle construct was performed in vitro by Strohman et al.¹⁷ More recently, free-standing constructs were microfabricated for skeletal muscle

Received: December 14, 2020

Accepted: February 8, 2021

Published: February 19, 2021



tissue engineering by Lam et al.¹⁸ Striated myotubes are key in skeletal muscles by driving the muscular movements. Notably, since the striated muscles are highly ordered and anisotropic tissues with interstitial structures, many studies have demonstrated micropatterned substrates such as grating/groove-like microstructures can also be utilized to perform cell behaviors studies in vitro.^{18–23} For example, parallel microgratings have been used to mimic the microstructure of the primary myotube layer.²⁴ In particular, it has been discovered that NPC cells can migrate to pterygoid muscles,⁶ which was histologic confirmed as striated muscles.²⁵ Further, cancer cachexia can cause myotube atrophy.²⁶ In fact, the myotube formation in pterygoid muscles is a concerned factor in clinical investigations.^{27,28} Therefore, in vitro analysis of cell behaviors on the micrograting topography can reveal the key attachment, spread, and migration of nasopharyngeal carcinoma cells on both the nearby and distant tissues. Recently, our group has reported preliminary characteristics of a nasopharyngeal cancerous cell line NPC43 on their stabilized cell spreading areas on micrograting structures,²⁹ yet other microtopography-mediated cell behaviors closely related to the metastatic tendency, for example, migration and spreading responsiveness, should be further investigated for our better understanding of the nasopharyngeal cancer metastasis in pterygoid muscle tissue.

In this work, we quantify the cell spreading and migration characteristics of NPC43 and another reference nasopharyngeal epithelial cell line NP460 growing on microgratings with different dimensions.³⁰ We apply the interference reflection microscopy (IRM) to visualize the transient cell attachment sites on the fabricated the grating microstructures. The findings can provide important insights on the expected behaviors of NPCs on tissue surfaces with different microtopography.

MATERIALS AND METHODS

Fabrication of Micro-Grating Substrates. The micrograting substrates were fabricated by replica molding of silicone (see Supporting Information (SI) Figure S1), whereas the molds made of silicon were fabricated by photolithography and deep reactive ion etch (DRIE, STS Deep Silicon Etcher, Surface Technology Systems, Newport, UK). Positive photoresist (AZ5214, AZ Electronic Materials, Branchburg, NJ) was first spin-coated on a silicon wafer and patterned by photolithography. The patterned silicon wafer was then processed by DRIE to generate micrograting structures with a depth of 15 μm . After removing the photoresist, the silicon wafer was silanized with vaporized (tridecafluoro-1,1,2,2-tetrahydrooctyl)-1-trichlorosilane (cat# 4488931, Sigma-Aldrich, St. Louis, MO) in a vacuum chamber. The polydimethylsiloxane polymer (PDMS, Sylgard-184, Dow Corning, Midland, MI) mixed with a 10% w/w curing agent was then spin-coated onto the fabricated silicon mold, followed by baking for 6 h at 80 °C. After peeling off the PDMS layer with grating structures from the silicon mold, such PDMS layer was bonded onto a confocal dish (SPL Life Science, Korea) using air plasma (PDC-002, Harrick Plasma, Ithaca, NY). We placed the confocal dish on a hot plate at 80 °C for 3 min to ensure the thorough cross-linkage of PDMS. After the substrate was attached to a confocal dish, the substrate was then exposed to air plasma to enhance the surface energy. The micrograting structure was then coated with fibronectin (FN, Sigma-Aldrich, St. Louis, MO) by applying 50 $\mu\text{g}/\text{mL}$ FN in the confocal dish for >1 h, followed by replacing the solution with PBS.

Cell Culture. Immortalized nasopharyngeal epithelial cell line NP460 and EBV-positive (EBV+ve) nasopharyngeal cancerous cell line NPC43 were obtained from research team of Prof. S. W. Tsao, University of Hong Kong. The NP460 cells were cultured in complete

Eplife medium (Thermo Fisher Scientific, Waltham, MA) and complete Defined Keratinocyte-SFM (serum-free medium) (Thermo Fisher Scientific, Waltham, MA) with a 1:1 mixture ratio, added with 100 units/mL penicillin and 100 $\mu\text{g}/\text{mL}$ streptomycin. NPC43 cells were maintained in Roswell Park Memorial Institute medium (RPMI-1640, American Type Culture Collection, Manassas, VA) containing 10% fetal bovine serum, 4 μM Y27632 dihydrochloride (Alexis, Lausen, Switzerland), 100 units/mL penicillin and 100 $\mu\text{g}/\text{mL}$ streptomycin. All cells were maintained in an incubator at 37 °C with 100% humidity and 5% CO_2 and the medium was changed every 2 days. When cell population reached 80% confluence, 0.25% trypsin-EDTA in phosphate buffered saline was used to resuspend cells, followed by subculture.

Fluorescence Staining. Cells were stained with CellTracker Green (CMFDA, Thermo Fisher Scientific, MA). The working dye solution was prepared by dissolving in Anhydrous dimethyl sulfoxide (DMSO) and diluted to a final working concentration of 10 μM in the serum-free medium. We first applied 0.25% trypsin-EDTA in phosphate-buffered saline (PBS; Sigma-Aldrich, St. Louis, MO) to resuspend cells. We then applied the working dye solution in a volumetric ratio of 1:1000 and incubate for 30 min. Hoechst 33342 (Thermo Fisher Scientific) with a concentration of 0.1 $\mu\text{g}/\text{mL}$ in PBS was applied for 15 min to stain DNA of nuclei. The cells were later centrifuged and rinsed in PBS for three times to remove the staining solution.

Scanning Electron Microscopy. The microfabricated substrates were mounted on stubs and sputtered with gold palladium using a versatile sputter coater (Quorum Q150TS, QUORUM Technologies, East Sussex, UK), followed by imaging under an environmental scanning electron microscope (FE-ESEM Quanta 450, Thermo Fisher Scientific, MA).

Image Capture. Interference reflection microscopy (IRM) was applied to observe the cell spreading and migration processes. The IRM was set up based on a laser scanning confocal microscopy (TCS-SP8, Leica Microsystems, Wetzlar, Germany). The Nikon Eclipse Ti-E microscope (Nikon, Tokyo, Japan) equipped with Chamlide TC incubator system perfused with 5% CO_2 at 37 °C was applied to capture the cell migration process. Microscopic images was captured every 3 s in the first hour for cell spreading and afterward every 5 min from 5 to 20 h for tracking the cell migration.

Image Processing and Data Analysis. Open source image processing software (ImageJ, National Institutes of Health) was adopted to process the microscopic image stacks. The cell spreading areas can be directly measured by ImageJ during while migration trajectory was manually measured by a tracking plugin installed in ImageJ. Cell spreading dynamics and migration trajectories were plotted with graphing and analysis software (Origin 2018, OriginLab Corporation). Pearson's correlation analysis was performed in numerical computing software (Matlab 2020a, MathWorks Corporation).

Statistics. *P*-values were calculated using the Student's *t* test in Excel (Microsoft, Seattle, WA), with *p* < 0.05 considered as statistically significant. Chi-Square tests were performed using GraphPad Prism 8 (GraphPad, San Diego, CA). All error bars presented in the figures without additionally mentioned are the standard errors.

RESULTS AND DISCUSSION

Micrograting Substrates. Microstructures with different topographic features (including geometrical features) are well-known to regulate cell behaviors.³¹ The geometrical features of microstructures can trigger cell–substrate interactions, subsequently affecting specific cellular behaviors depending on the cell type, pattern size, geometry and other factors of the substrates.³² In this work, we have designed three surface profiles, including two micrograting structures (as shown in Figure 1a) and one flat surface on each microfabricated substrate. These substrates were fabricated using replica

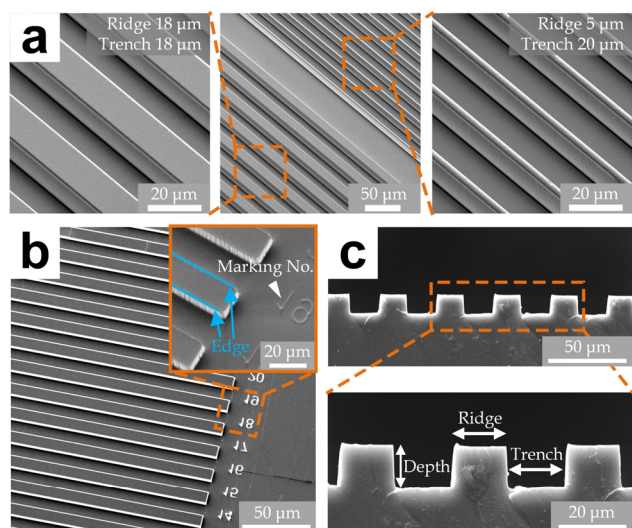


Figure 1. (a) SEM images of microtopography with different grating structures. (b) Grating structures with numbering markers aside. Inset: an enlarged edge region. (c) Side-view of the micrograting structures. Inset: definition of depth, ridge, and trench.

molding of polydimethylsiloxane (PDMS) as described in [Materials and Methods](#). Further, the microgratings are labeled by the numbering markers located aside as shown in [Figure 1b](#), in order to track individual cells at different time points for their spreading and migration behaviors. The outer surfaces are defined as “ridges” whereas the inner surfaces are defined as “trenches” as illustrated in [Figure 1c](#). We adopt two designs: one with a 5 μm ridge width and a 20 μm trench width, and the other one with the ridge and trench widths both 18 μm . We have chosen 18 and 5 μm as the ridge width to match the diameters of normal myotubes and recessive myotubes, respectively.^{33,34} It is expected that most of the individual NP460/NPC43 cells lie on one “ridge-edge” for the “18 μm ” region and two “ridge-edges” for the “5 μm ” region, as reported in our previous studies.^{29,35} Notably, in this study, we only select the cells in contact with one edge of the 18 μm -ridges and those in contact with both edges of the 5 μm -ridges in all the data analysis; and therefore we named those cells as “monoedge” and “biedge” attachment cases.

Cell Spreading. Apparently, cell spreading occurs before migration.³⁶ As discussed previously, we configured interference reflection microscopy (IRM) using a laser confocal microscope (SI [Figure S2a](#)) to observe temporal spatial cell–substrate attachment dynamics. To ensure the better laser penetration ability over the sample, an incident laser with wavelength of 638 nm was selected to achieve higher laser penetration capability via cells and substrates, and hence better imaging quality. We adopted a 63 \times oil immersion objective for achieving a resolution of 120 nm/pixel for the microscopic images. We used two photomultiplier tubes (PMTs), with one for capturing the interference reflection light and visualizing the interface contact area and the other one for capturing the transmission light for the relative locations and diameters of cells.

Before seeding the cells, we rinsed a confocal dish precoated with fibronectin with 100% ethanol, 50% ethanol, and then phosphate-buffered saline (PBS) for sterilization. We then seeded NP460/NPC43 on the microfabricated substrate at a density of $\sim 3 \times 10^3$ cells/ cm^2 . IRM images and transmission

images were then captured every 3 s for 1 h; and the representative images are provided in [Figure 2](#). It should be

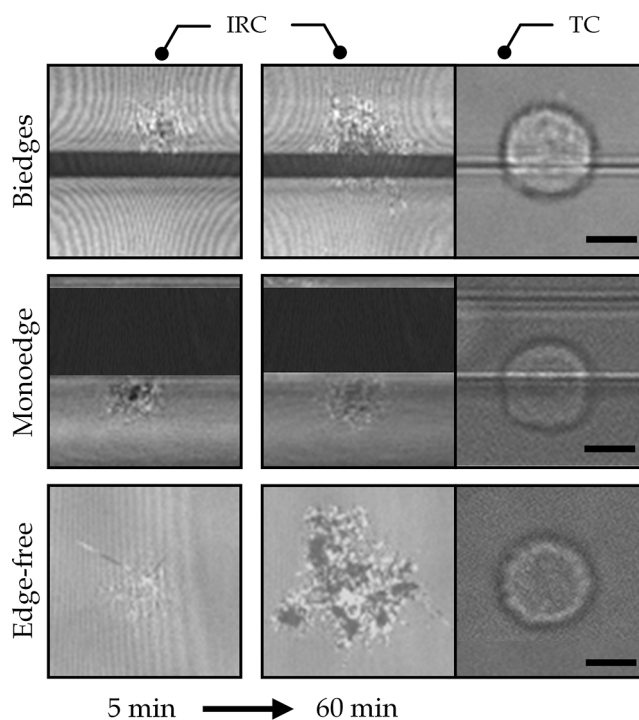


Figure 2. Representative cell spreading snapshots of NP460 cells for the biedge, monoedge and edge-free contact modes at 5 and 60 min, observed through interference reflection channels (IRC) and the corresponding transmission channels (TC) of the IRM (scale bar: 10 μm).

mentioned that IRM can only reveal the cell attachment over a horizontal focal plan,³⁷ partial spreading areas of the cells on the microgratings (either the ridge or trench region) can be observed. Hence, we estimated the cell boundaries and the spreading areas. The area ratios of cells on ridges or trenches were first observed from the transmission channel, denoted as A_1 and A_2 , respectively. We then captured the cell-ridge attachment areas on the grating ridges using IRM as A_4 , followed by predicting the trench-overlapping areas $A_3 = A_1/A_2 \times A_4$ and the total cell spreading areas $A_{\text{sum}} = A_3 + A_4$.^{38–40} The spreading areas of NP460 and NPC43 for the biedge, monoedge and edge-free modes over the first hour of attachment are provided in [Figure 3a](#). As summarized in [Figure 3b](#), the average equilibrium contact areas of NP460 cells for the biedge, monoedge and edge-free modes are $133.54 \pm \text{SE } 3.17 \mu\text{m}^2$, $125.68 \pm \text{SE } 1.92 \mu\text{m}^2$, $181.44 \pm \text{SE } 8.29 \mu\text{m}^2$, respectively. The average equilibrium contact areas of NPC43 for the biedge, monoedge and edge-free modes are $112.15 \pm \text{SE } 2.58 \mu\text{m}^2$, $117.77 \pm \text{SE } 3.94 \mu\text{m}^2$, $171.24 \pm \text{SE } 3.69 \mu\text{m}^2$, respectively. On the other hand, we have quantified the cell diameters by taking microscopic pictures of cells in suspension with the values of $13.84 \pm \text{SE } 0.21 \mu\text{m}$ for NP460 cells ($N = 40$) and $14.18 \pm \text{SE } 0.25 \mu\text{m}$ for NPC43 cells ($N = 40$), with no significant difference ($p = 0.18$) on the cell diameters between two cell lines. Therefore, NP460 cells exhibited slightly higher equilibrium contact area than NPC43 for all the biedge, monoedge and edge-free modes.

We applied the widely adopted hyperbolic tangent function^{41–43} to fit with the measured cell spreading area

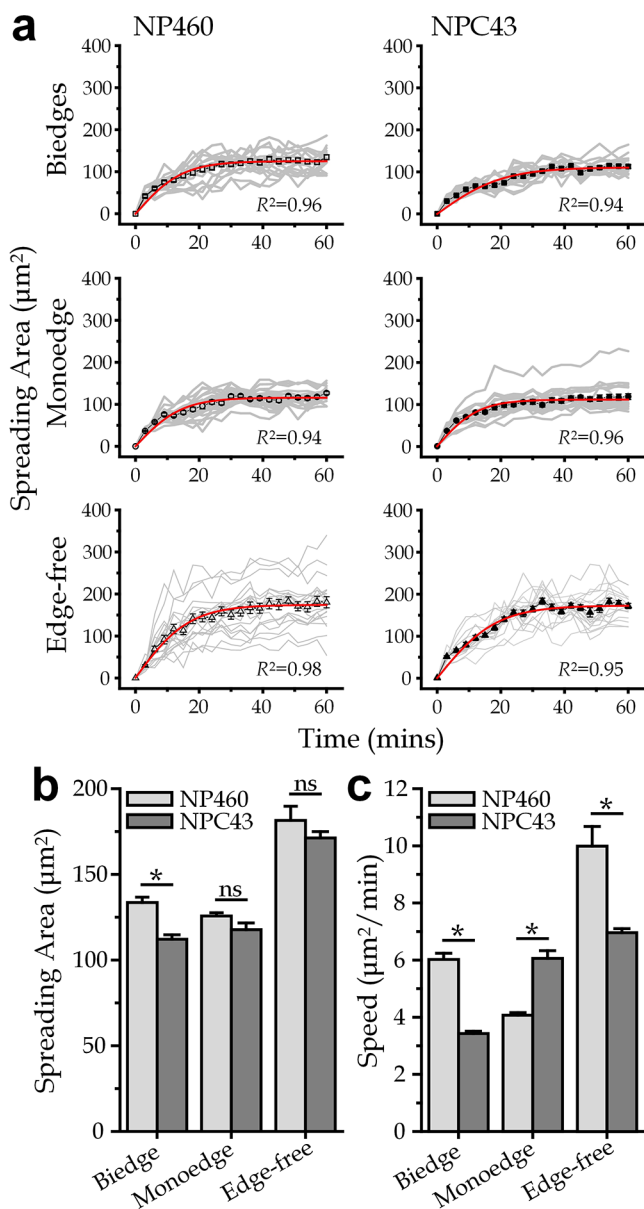


Figure 3. (a) Transient cell spreading areas of NP460 and NPC43 cells with monoedge, biedge and edge-free contacts ($N = 40$ for each case). Gray lines indicate individual cells and red lines are fitting lines of the average spreading area over time. (b) Calculated cell equilibrium spreading area and (c) average spreading speeds for different edge-contact modes. $N = 40$ for all cases. * indicates $p < 0.05$.

$A(t)$ over time t as $A(t) = A_{eq} \cdot \tanh(t/\tau)$, where A_{eq} and τ are constants as indicated in Figure 3a. Apparently, we may define da/dt at $t = 0$ as the initial spreading speed of the attachment area, which can be easily obtained with the fitted parameters as A_{eq}/τ . The average spreading speeds are $6.02 \pm SE 0.22 \mu\text{m}^2/\text{min}$, $4.07 \pm SE 0.09 \mu\text{m}^2/\text{min}$, and $9.99 \pm SE 0.69 \mu\text{m}^2/\text{min}$ for NP460 cells spreading for the biedge, monoedge and edge-free modes, respectively. The average spreading speeds are $3.43 \pm SE 0.08 \mu\text{m}^2/\text{min}$, $6.06 \pm SE 0.27 \mu\text{m}^2/\text{min}$ and $6.96 \pm SE 0.14 \mu\text{m}^2/\text{min}$ for NPC43 cells spreading for the biedge, monoedge and edge-free modes, respectively.

Cell Migration. Characterizing the single cell migration behaviors could reveal the malignant tendency of the cancer cells.⁴⁴ The cells were observed under an incubator-equipped

microscope, as shown in SI Figure S2b. We monitored the cell migration by taking time-lapsed microscopic images for every 5 min during the observation period from 5 to 20 h after cell seeding. Only the period between 5–20 h after cell seeding and while the cells were still with the desired contact modes with the ridge-edges was analyzed in order to reflect better the stabilized cell migration behaviors for the corresponding edge-contact modes. The edge-free case had ~ 15 h of the contact period for both cells. The biedge contact periods of NP460 cell and NPC43 cells are $7.21 \pm SE 0.78$ h and $4.16 \pm SE 0.66$ h, respectively, whereas the monoedge contact periods of NP460 cell and NPC43 cells are $12.39 \pm SE 0.83$ h and $11.57 \pm SE 1.09$ h, respectively. The “biedge” NPC43 cells exhibited the shortest contact period among all the concerned cases.

In addition, we quantified the cell migration properties as the migration distance and directionality. The migration distance was calculated by summing up the migration distances for all time-steps, that is, all the lengths of hidden lines as illustrated in Figure 4c, throughout the observation period. The directionality was considered as the orientation between the start and end positions of the migration trajectory, as indicated as φ in Figure 4c. The migration trajectories for NP460 and NPC43 cells on different substrates are summarized in Figure 4a. These results indicate that NPC43 cells migrated faster than NP460 cells in general. Recalling that the spreading areas of NPC43 cells are generally slightly smaller than those of NP460 cells (Figure 3b), such difference in migration speed was not caused by the physical scaling. NP460 cells have a relatively lower migration speed (Figure 4b) for the monoedge case than that for the biedge case. It appears that there may be statistical correspondence with the cell spreading area and speed as discussed previously in Figure 3b,c. Furthermore, the migration directionality of NP460 and NPC43 cells for different contact cases are provided in Figure 4d. Our results reflect that both cell types could be well-guided to migrate along the edge/ridge direction ($\varphi \sim 0^\circ$ or 180°) for the monoedge case, agreeing with observations from others' works,⁴⁵ whereas the cells with the biedge contact had a dominant migration direction of $\sim 90^\circ$. The edge-free contact case obviously did not exhibit any directional preference as the direction was set arbitrarily. To distinguish whether the cell migration directionality of NP460 and NPC43 cells on different contact modes has a directional preference, we performed the Chi-Square test by comparing the experimental results (Figure 4d) with a “random” distribution, whose possibility is 0.1667 for each of the six angular groups. The results indicated significant differences and hence directional preference for monoedge and biedge cases ($p \ll 0.01$) and no statistical significance for edge-free NP460 ($\chi^2 = 25.05$, $p = 0.7225$) and NPC43 ($\chi^2 = 28.79$, $p = 0.5284$) cells. It can also be observed that the preferred directions for the monoedge and biedge cases were around $\varphi = 0^\circ/180^\circ$ and $\varphi = 90^\circ$, respectively, with respect to the micrograting orientation. Though the average directions for both monoedge and biedge cases are around 90° , such preferred direction can be revealed by the value of deviation as shown in Figure 4e. The deviation of NP460 cell directionality for the monoedge case ($64.26^\circ \pm SE 3.44^\circ$) is significantly higher than that for the biedge case ($33.09^\circ \pm SE 4.13^\circ$). Likewise, NPC43 cells show a higher deviation of directionality for the monoedge case ($69.01^\circ \pm SE 4.01^\circ$) than that of the biedge case ($32.46^\circ \pm SE 4.26^\circ$). Overall, these results indicate that the cells exhibit the preference of migration along the grating orientation for the

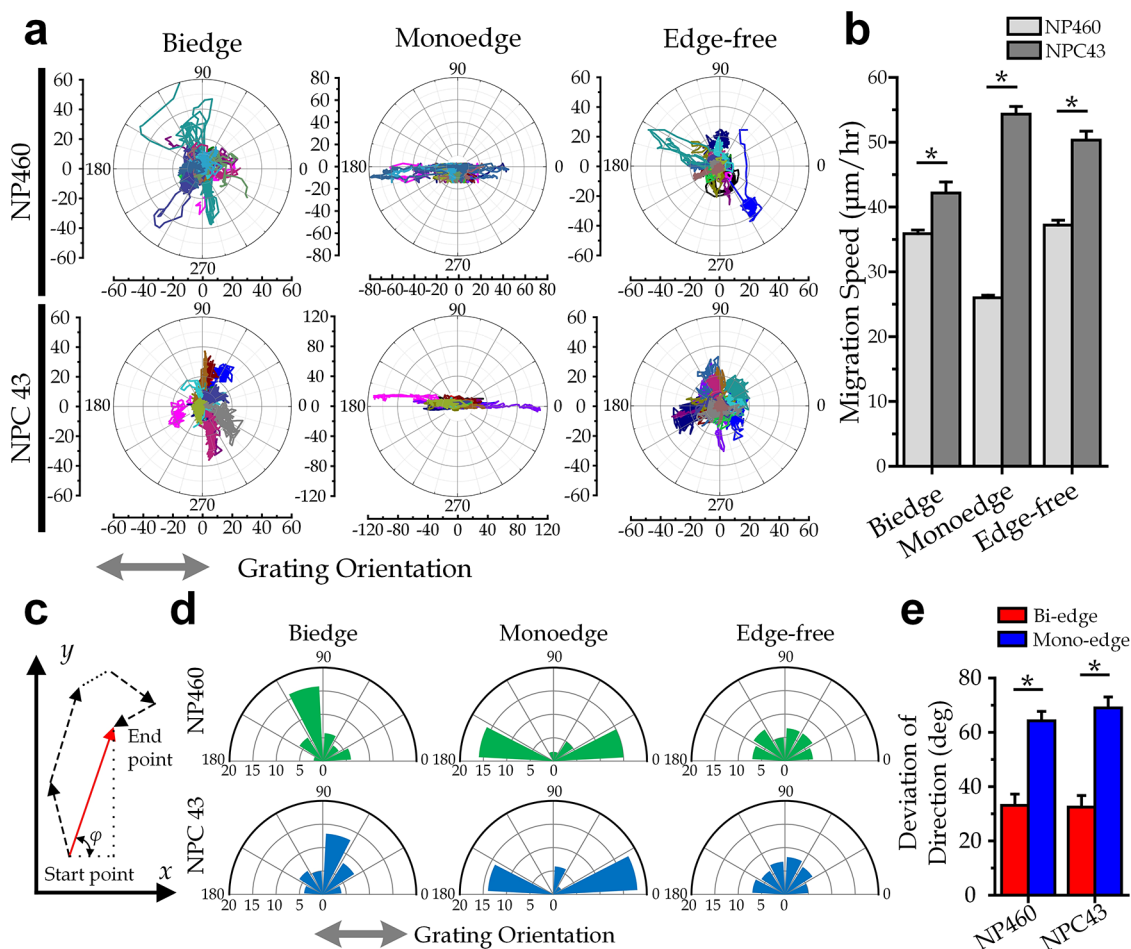


Figure 4. (a) Cell migration trajectories on edge-contact modes. Note that the orientation of the edge-free cells is arbitrary as there is no micrograting. (b) Cell migration speeds for different edge-contact modes. $N = 40$ for all cases. * indicates $p < 0.05$. (c) Calculation of cell migration length and the definition of the migration directionality as the angle φ . (d) Statistics of the directionality of NP460 and NPC43 cells. (e) Deviations of directionality of the NP460 and NPC43 cells. * indicates $p < 0.05$.

monoedge case, whereas perpendicular to the grating orientation for the biedge case.

It is worth noting that such migration behaviors and cell morphology during migration process can be affected by the grating size. Our previous work has performed cell migration study by using $2/2 \mu\text{m}$ wide ridge/trench with $1 \mu\text{m}$ depth microgratings to guide NPC43 and NP460 cells migration.⁴⁶ The reported results indicate that cells are adherent on grating substrate by crossing several ridges and trenches and both NPC43 and NP460 cells exhibited the preference of elongation morphology along the grating orientation, whereas filopodia can be observed only on NPC43 cells. As shown in SI Figure S6, cell morphology varies under different edge contact modes. Besides, the calculated cell migration speeds for NPC43 and NP460 cells on the microgratings with $2 \mu\text{m}$ ridge, trench, and $1 \mu\text{m}$ depth are significant slower than those on the monoedge, biedge, and edge-free substrates as used in this work.

Together, these results suggest that cell contact conditions can affect the cell migration behaviors. Considering the monoedge case, the cells majorly migrate along the microstructure direction, implicating that the cells may prefer maintaining the contact condition. On the other hand, cells in the biedge contact tend to migrate perpendicularly to the micropattern orientation, possibly reflecting that the biedge contact is not a favorable contact condition for the cells. As the

cell contact modes can affect both the cell spreading and migration properties, there may be correspondence between these cell properties as well. Furthermore, cell migration is a complex process that includes multiple essential intracellular cytoskeletal dynamics, such as actin filaments (F-actin) polymerization and depolymerization, focal adhesion (FA) formation, and disassembly.⁴⁷ Moreover, proteins related to FA (e.g., focal adhesion kinase (FAK), paxillin, vinculin) link the integrin receptors with the actin cytoskeleton and also regulate actin polymerization and contractility. Consequently, mediate the adhesion formation and regulate cell migration.⁴⁸ Previous studies also reported that mean size of FA was highly predictive of cell migration speed.⁴⁹ The more detailed investigation on the cytoskeletal dynamics in the future should provide very important information and insights explaining the observed cell migration behaviors and their correlations with the cell initial spreading.

Correlations between Spreading and Migration. We have examined the correlations between cell spreading and migration properties for different cell contact case. Cell migration is known to correlate to the cell attachment area in various microenvironments.^{49–51} Here, we consider two spreading parameters (i.e., stabilized spreading area and spreading speed) and one migration parameter (i.e., migration speed). We obtained the corresponding Pearson's correlation

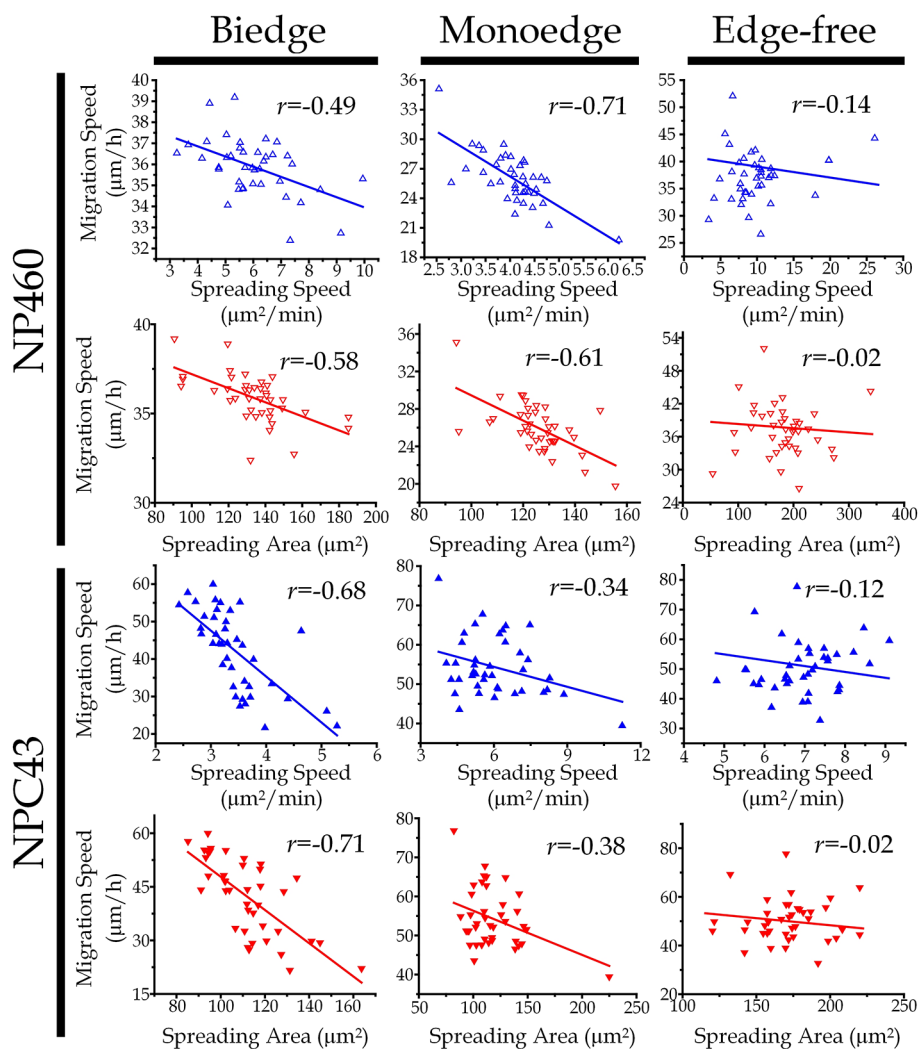


Figure 5. Correlations of cell migration speed versus the cell spreading area and speed.

coefficient (r) as it is widely used to represent correlations between cell properties,⁵² and the results are shown in Figure 5. It appears that monoedge and biedge cells generally have larger r -values than the edge-free cells, implying that the cells attaching on the microgratings can reveal different spreading-migration correlations. There is likely a negative correlation between the cell spreading area and the migration speed, agreeing with a previous study.⁵³ The cells associated with faster cell spreading tend to express the lower migration speed.

Collectively, this research demonstrates that the microgratings can be applied to discover specific cell spreading and migration behaviors. The results on the nasopharyngeal cells could have the capability to determine their migration direction upon the microtopographic environment. The 18 μm -ridge microgratings appear to more favorable than the 5 μm -ridge ones to the cells. In particular, the nasopharyngeal cancer cells can migrate significantly faster than the nasopharyngeal cells on the 18 μm -ridge substrates. In view of the fact that the myotubes have an average diameter of around 18 μm ,³³ our results can explain, to a certain extent, the colonization of nasopharyngeal cancer cells and the subsequent secondary tumor formation on pterygoid muscles. Additionally, the micrograting structures can be further applied for mimicking the muscular microtubes under different conditions. For example, a progressive muscle atrophy disease called

Duchenne muscular dystrophy, which has a high incidence rate in male newborns,^{54,55} causes muscle weakening and muscular malformations through the formation of thinner myotubes with a diameter of $\sim 5 \mu\text{m}$.³⁴

CONCLUSION

We report the spreading and migration behaviors of non-cancerous (NP460) and cancerous (NPC43) human nasopharyngeal cells on microfabricated gratings based on the contact modes with the grating edges, that is, monoedge, biedge, and edge-free contacts. We successfully utilized IRM to quantify the cell spreading dynamics during the first hour after cell seeding. The cells were then monitored under a microscopy for their migration trajectories and the corresponding migration speed and directionality. Results indicate that the cell migration speed does not depend to the cell spreading properties (area and spreading speed) without contact with the grating edges, reflected by the very weak correlations ($|r| < 0.14$). Yet, the micrograting edges can help reveal the correlations ($-0.71 < r < -0.34$) between the migration speed and the spreading area and speed for cells in contact with the edges. Specifically, the 18 μm -ridge microgratings can guide the migration direction of the selected cells. This may explain, to a certain extent, the preferred nasopharyngeal cancer spreading to the nearby pterygoid muscles, in which the

myotubes have an average diameter of $\sim 18 \mu\text{m}$. The cell spreading and migration study on microgratings can be further applied to investigate muscular tissue engineering, and more general cell research.

■ ASSOCIATED CONTENT

SI Supporting Information

The Supporting Information is available free of charge at <https://pubs.acs.org/doi/10.1021/acsabm.0c01610>.

Fabrication process of microgratings, cell observation setting up, microgratings height characterization, definition of edge mode, cell–substrate interaction, and cell migration morphology (PDF)

■ AUTHOR INFORMATION

Corresponding Authors

Raymond H. W. Lam – Department of Biomedical Engineering and Centre for Biosystems, Neuroscience, and Nanotechnology, City University of Hong Kong, Kowloon, Hong Kong; City University of Hong Kong Shenzhen Research Institute, Shenzhen, China; orcid.org/0000-0002-5188-3830; Phone: +852-3442-8577; Email: rhwlam@cityu.edu.hk; Fax: +852-3442-0172

Stella W. Pang – Department of Electrical Engineering and Centre for Biosystems, Neuroscience, and Nanotechnology, City University of Hong Kong, Kowloon, Hong Kong; orcid.org/0000-0002-4330-0877; Phone: +852-3442-9853; Email: pang@cityu.edu.hk; Fax: +852-3442-0562

Authors

Yi Liu – Department of Biomedical Engineering, City University of Hong Kong, Kowloon, Hong Kong; City University of Hong Kong Shenzhen Research Institute, Shenzhen, China; orcid.org/0000-0002-9879-2995

Jifeng Ren – Department of Biomedical Engineering, City University of Hong Kong, Kowloon, Hong Kong; City University of Hong Kong Shenzhen Research Institute, Shenzhen, China; School of Biomedical Engineering, Capital Medical University, Beijing 100069, China

Ruolin Zhang – Department of Electrical Engineering, City University of Hong Kong, Kowloon, Hong Kong; Department of Biomedical Engineering, The Hong Kong Polytechnic University, Hung Hom, Hong Kong

Shuhuan Hu – BGI-Shenzhen, Shenzhen 518083, Guangdong, China; orcid.org/0000-0002-4163-1242

Complete contact information is available at: <https://pubs.acs.org/doi/10.1021/acsabm.0c01610>

Author Contributions

[¶]These authors contributed equally to this work

Notes

The authors declare no competing financial interest.

■ ACKNOWLEDGMENTS

We acknowledge financial supports from the National Natural Science Foundation of China (NSFC Grant 31770920), and Hong Kong Research Grant Council (General Research Grant 11216220 and Collaborative Research Fund C1013-15GF).

■ REFERENCES

(1) Ho, J. H. An epidemiologic and clinical study of nasopharyngeal carcinoma. *Int. J. Radiat. Oncol., Biol., Phys.* **1978**, *4* (3–4), 183–198.

(2) Liao, W.; Tian, M.; Chen, N. Characteristic And Novel Therapeutic Strategies Of Nasopharyngeal Carcinoma With Synchronous Metastasis. *Cancer Manage. Res.* **2019**, *11*, 8431.

(3) King, A. D.; Bhatia, K. S. S. Magnetic resonance imaging staging of nasopharyngeal carcinoma in the head and neck. *World journal of radiology* **2010**, *2* (5), 159.

(4) Li, W.-F.; Sun, Y.; Chen, M.; Tang, L.-L.; Liu, L.-Z.; Mao, Y.-P.; Chen, L.; Zhou, G.-Q.; Li, L.; Ma, J. Locoregional extension patterns of nasopharyngeal carcinoma and suggestions for clinical target volume delineation. *Aizheng* **2012**, *31* (12), S79.

(5) Xiao, Y.; Pan, J.; Chen, Y.; Lin, S.; Zong, J.; Chen, Y.; Fang, Y. The prognosis of nasopharyngeal carcinoma involving masticatory muscles: a retrospective analysis for revising T subclassifications. *Medicine* **2015**, *94* (4), No. e420.

(6) Pan, J. J.; Ng, W. T.; Zong, J. F.; Chan, L. L.; O'Sullivan, B.; Lin, S. J.; Sze, H. C.; Chen, Y. B.; Choi, H. C.; Guo, Q. J. Proposal for the 8th edition of the AJCC/UICC staging system for nasopharyngeal cancer in the era of intensity-modulated radiotherapy. *Cancer* **2016**, *122* (4), 546–558.

(7) Almomani, M. H.; Zulfiqar, H.; Nagalli, S., Nasopharyngeal Carcinoma (NPC, Lymphoepithelioma). *StatPearls [Internet]* **2020**, PMID: 32644348, NBK558922.1289

(8) Fu, S.; Li, J.-s.; Dias-Ribeiro, E.; Freire, J. C. P.; Sun, S.; Fan, S. Aggressive Surgical Resection of Enormous Cervical Metastasis from Nasopharyngeal Carcinoma. *Acta Stomatol. Croat.* **2019**, *53* (2), 168–173.

(9) Hallak, B.; Morrison, M.; Kohler, R.; Bouayed, S. Deep radiation-induced ulcer following nasopharyngeal carcinoma: surgical management. *BMJ. Case Reports CP* **2019**, *12* (11), No. e230700.

(10) Chen, M.-Y.; Mai, H.-Q.; Sun, R.; Guo, X.; Zhao, C.; Hong, M.-H.; Hua, Y.-J. Clinical findings and imaging features of 67 nasopharyngeal carcinoma patients with postradiation nasopharyngeal necrosis. *Aizheng* **2013**, *32* (10), 533.

(11) Goh, A.; Yeh, C.-C.; Lei, K. F. Visualization and Quantification of 3D Tumor Cell Migration under Extracellular Stimulation. *ACS Applied Bio Materials* **2020**, *3* (3), 1506–1513.

(12) Huang, C.-H.; Lei, K. F. Impedimetric quantification of migration speed of cancer cells migrating along a Matrigel-filled microchannel. *Anal. Chim. Acta* **2020**, *1121*, 67–73.

(13) Guan, X. Cancer metastases: challenges and opportunities. *Acta Pharm. Sin. B* **2015**, *5* (5), 402–418.

(14) Zervantonakis, I. K.; Hughes-Alford, S. K.; Charest, J. L.; Condeelis, J. S.; Gertler, F. B.; Kamm, R. D. Three-dimensional microfluidic model for tumor cell intravasation and endothelial barrier function. *Proc. Natl. Acad. Sci. U. S. A.* **2012**, *109* (34), 13515–13520.

(15) Chiang, S. P.; Cabrera, R. M.; Segall, J. E. Tumor cell intravasation. *American Journal of Physiology-Cell Physiology*. *American Journal of Physiology-Cell Physiology* **2016**, *311* (1), C1–C14.

(16) Lewis, M. R. Rhythmical contraction of the skeletal muscle tissue observed in tissue cultures. *Am. J. Physiol.* **1915**, *38* (1), 153–161.

(17) Strohmman, R. C.; Bayne, E.; Spector, D.; Obinata, T.; Micou-Eastwood, J.; Maniotis, A. Myogenesis and histogenesis of skeletal muscle on flexible membranes in vitro. *In Vitro Cell. Dev. Biol.* **1990**, *26* (2), 201–208.

(18) Lam, M. T.; Huang, Y.-C.; Birla, R. K.; Takayama, S. Microfeature guided skeletal muscle tissue engineering for highly organized 3-dimensional free-standing constructs. *Biomaterials* **2009**, *30* (6), 1150–1155.

(19) Altomare, L.; Riehle, M.; Gadegaard, N.; Tanzi, M.; Farè, S. Microcontact printing of fibronectin on a biodegradable polymeric surface for skeletal muscle cell orientation. *Int. J. Artif. Organs* **2010**, *33* (8), 535–543.

(20) Charest, J. L.; García, A. J.; King, W. P. Myoblast alignment and differentiation on cell culture substrates with microscale topography and model chemistries. *Biomaterials* **2007**, *28* (13), 2202–2210.

- (21) Zhao, Y.; Zeng, H.; Nam, J.; Agarwal, S. Fabrication of skeletal muscle constructs by topographic activation of cell alignment. *Biotechnol. Bioeng.* **2009**, *102* (2), 624–631.
- (22) Jana, S.; Levegood, S. K. L.; Zhang, M. Anisotropic materials for skeletal-muscle-tissue engineering. *Adv. Mater.* **2016**, *28* (48), 10588–10612.
- (23) Beunk, L.; Brown, K.; Nagtegaal, I.; Friedl, P.; Wolf, K. Cancer invasion into musculature: mechanics, molecules and implications. In *Seminars in cell & developmental biology*; Elsevier, 2019; pp 36–45.
- (24) Guex, A. G.; Birrer, D. L.; Fortunato, G.; Tevæarai, H. T.; Giraud, M.-N. Anisotropically oriented electrospun matrices with an imprinted periodic micropattern: a new scaffold for engineered muscle constructs. *Biomed. Mater.* **2013**, *8* (2), 021001.
- (25) Koritzer, R. T.; Suarez, F. Accessory medial pterygoid muscle. *Cells Tissues Organs* **1980**, *107* (4), 467–473.
- (26) Ge, Z.; Liu, D.; Shang, Y.; Li, Y.; Chen, S.-z. Magnolol inhibits myotube atrophy induced by cancer cachexia through myostatin signaling pathway in vitro. *Journal of Natural Medicines* **2020**, *74* (4), 741–749.
- (27) Carranza, M. L.; Carda, C.; Simbrón, A.; Quevedo, M.; Celaya, G.; De Ferraris, M. Morphology of the lateral pterygoid muscle associated to the mandibular condyle in the human prenatal stage. *Acta odontologica latinoamericana: AOL* **2006**, *19* (1), 29.
- (28) Benoît, R.; Baudoin, C. A morphometric investigation of myotube formation in rabbit embryo medial pterygoid muscle. *J. Dent. Res.* **1996**, *75* (11), 1835–1841.
- (29) Lam, B. P.; Cheung, S. K.; Lam, Y. W.; Pang, S. W. Microenvironmental topographic cues influence migration dynamics of nasopharyngeal carcinoma cells from tumour spheroids. *RSC Adv.* **2020**, *10* (48), 28975–28983.
- (30) Tsang, C. M.; Zhang, G.; Seto, E.; Takada, K.; Deng, W.; Yip, Y. L.; Man, C.; Hau, P. M.; Chen, H.; Cao, Y.; Lo, K. W. Epstein-Barr virus infection in immortalized nasopharyngeal epithelial cells: Regulation of infection and phenotypic characterization. *Int. J. Cancer* **2010**, *127* (7), 1570–1583.
- (31) Nikkhah, M.; Edalat, F.; Manoucheri, S.; Khademhosseini, A. Engineering microscale topographies to control the cell-substrate interface. *Biomaterials* **2012**, *33* (21), 5230–5246.
- (32) Ermiş, M.; Antmen, E.; Hasirci, V. Micro and Nanofabrication methods to control cell-substrate interactions and cell behavior: A review from the tissue engineering perspective. *Bioactive materials* **2018**, *3* (3), 355–369.
- (33) Van der Meijden, K.; Bravenboer, N.; Dirks, N.; Heijboer, A.; Den Heijer, M.; De Wit, G.; Offringa, C.; Lips, P.; Jaspers, R. Effects of 1, 25 (OH) 2D3 and 25 (OH) D3 on C2C12 myoblast proliferation, differentiation, and myotube hypertrophy. *J. Cell. Physiol.* **2016**, *231* (11), 2517–2528.
- (34) Nesmith, A. P.; Wagner, M. A.; Pasqualini, F. S.; O'Connor, B. B.; Pincus, M. J.; August, P. R.; Parker, K. K. A human in vitro model of Duchenne muscular dystrophy muscle formation and contractility. *J. Cell Biol.* **2016**, *215* (1), 47–56.
- (35) Tang, Q. Y.; Tong, W. Y.; Shi, J.; Shi, P.; Lam, Y. W.; Pang, S. W. Influence of engineered surface on cell directionality and motility. *Biofabrication* **2014**, *6* (1), 015011.
- (36) Trepāt, X.; Chen, Z.; Jacobson, K. Cell migration. *Comprehensive Physiology* **2012**, *2* (4), 2369–2392.
- (37) Verschueren, H. Interference reflection microscopy in cell biology: methodology and applications. *J. Cell Sci.* **1985**, *75* (1), 279–301.
- (38) Fardin, M.; Rossier, O.; Rangamani, P.; Avigan, P.; Gauthier, N.; Vonnegut, W.; Mathur, A.; Hone, J.; Iyengar, R.; Sheetz, M. Cell spreading as a hydrodynamic process. *Soft Matter* **2010**, *6* (19), 4788–4799.
- (39) Zemel, A.; Rehfeldt, F.; Brown, A.; Discher, D.; Safran, S. Cell shape, spreading symmetry, and the polarization of stress-fibers in cells. *J. Phys.: Condens. Matter* **2010**, *22* (19), 194110.
- (40) Greiner, A. M.; Chen, H.; Spatz, J. P.; Kemkemer, R. Cyclic tensile strain controls cell shape and directs actin stress fiber formation and focal adhesion alignment in spreading cells. *PLoS One* **2013**, *8* (10), No. e77328.
- (41) Chamaraux, F.; Fache, S.; Bruckert, F.; Fourcade, B. Kinetics of cell spreading. *Phys. Rev. Lett.* **2005**, *94* (15), 158102.
- (42) Chamaraux, F.; Ali, O.; Keller, S.; Bruckert, F.; Fourcade, B. Physical model for membrane protrusions during spreading. *Phys. Biol.* **2008**, *5* (3), 036009.
- (43) Hui, K. L.; Wang, C.; Grooman, B.; Wayt, J.; Upadhyaya, A. Membrane dynamics correlate with formation of signaling clusters during cell spreading. *Biophys. J.* **2012**, *102* (7), 1524–1533.
- (44) Zhao, L.; Guo, T.; Wang, L.; Liu, Y.; Chen, G.; Zhou, H.; Zhang, M. Tape-assisted photolithographic-free microfluidic chip cell patterning for tumor metastasis study. *Anal. Chem.* **2018**, *90* (1), 777–784.
- (45) Dalton, B. A.; Walboomers, X. F.; Dziegielewski, M.; Evans, M. D.; Taylor, S.; Jansen, J. A.; Steele, J. G. Modulation of epithelial tissue and cell migration by microgrooves. *J. Biomed. Mater. Res.* **2001**, *56* (2), 195–207.
- (46) Liu, Z.; Zhang, W.; Pang, S. W. Migration of immortalized nasopharyngeal epithelia and carcinoma cells through porous membrane in 3D platforms. *Biosci. Rep.* **2020**, *40* (6), BSR20194113.
- (47) Vicente-Manzanares, M.; Webb, D. J.; Horwitz, A. R. Cell migration at a glance. *J. Cell Sci.* **2005**, *118* (21), 4917–4919.
- (48) Chen, S.; Hourwitz, M. J.; Campanello, L.; Fourkas, J. T.; Losert, W.; Parent, C. A. Actin Cytoskeleton and Focal Adhesions Regulate the Biased Migration of Breast Cancer Cells on Nanoscale Asymmetric Sawteeth. *ACS Nano* **2019**, *13* (2), 1454–1468.
- (49) Kim, D. H.; Wirtz, D. Focal adhesion size uniquely predicts cell migration. *FASEB J.* **2013**, *27* (4), 1351–1361.
- (50) Mohammed, D.; Charras, G.; Vercruyse, E.; Versaavel, M.; Lantoiné, J.; Alaimo, L.; Bruyère, C.; Luciano, M.; Glinel, K.; Delhaye, G. Substrate area confinement is a key determinant of cell velocity in collective migration. *Nat. Phys.* **2019**, *15* (8), 858–866.
- (51) Liang, E. I.; Mah, E. J.; Yee, A. F.; Digman, M. A. Correlation of focal adhesion assembly and disassembly with cell migration on nanotopography. *Integrative biology* **2017**, *9* (2), 145–155.
- (52) Benesty, J.; Chen, J.; Huang, Y.; Cohen, I. Pearson correlation coefficient. In *Noise Reduction in Speech Processing*; Springer: Berlin, Heidelberg, 2009; pp 1–4.
- (53) Webb, K.; Hlady, V.; Tresco, P. A. Relationships among cell attachment, spreading, cytoskeletal organization, and migration rate for anchorage-dependent cells on model surfaces. *J. Biomed. Mater. Res.* **2000**, *49* (3), 362–368.
- (54) Nozoe, K. T.; Akamine, R. T.; Mazzotti, D. R.; Polesel, D. N.; Grossklauss, L. F.; Tufik, S.; Andersen, M. L.; Moreira, G. A. Phenotypic contrasts of Duchenne Muscular Dystrophy in women: Two case reports. *Sleep Science* **2016**, *9* (3), 129–133.
- (55) Schram, G.; Fournier, A.; Leduc, H.; Dahdah, N.; Therien, J.; Vanasse, M.; Khairy, P. All-cause mortality and cardiovascular outcomes with prophylactic steroid therapy in Duchenne muscular dystrophy. *J. Am. Coll. Cardiol.* **2013**, *61* (9), 948–954.